Composite behavior of lath-martensite steels induced by plastic strain, a new paradigm for the elastic-plastic response of martensitic steels

Tamás Ungár[1,3*&], Stefanus Harjo[2*], Takuro Kawasaki[2], Yo Tomota[4**], Gábor Ribárik[1,3] and Zengmin Shi[5]

[1]Department of Materials Physics, Eötvös University, Budapest, PO Box 32, H-1518, Hungary
[2]J-PARC Center, Japan Atomic Energy Agency, Tokai-mura, Naka-gun, Ibaraki 319-1195, Japan
[3]Laboratory of Excellence "DAMAS", Université de Lorraine, Nancy-Metz, F-57045 Metz, France
[4]Graduate School of Science and Engineering, Ibaraki University, 4-12-1 Nakanarusawa, Hitachi, Ibaraki, 316-8511, Japan
[5]College of Materials and Chemical Engineering, China Three Gorges University, Yichang 443002, PR China

*These authors contributed equally
** now at National Institute for Materials Science, 1-2-1 Sengen, Tsukuba, Ibaraki, 305-0047, Japan

ABSTRACT

Based on high-resolution neutron diffraction experiments we will show that in lath-martensite steels the initially homogeneous dislocation structure, i.e. homogeneous on the length scale of grain size, is disrupted by plastic deformation, which, in turn, produces a composite on the length scale of martensite lath-packets. The diffraction patterns of plastically strained martensitic steel reveal characteristically asymmetric peak profiles in the same way as has been observed in materials with heterogeneous dislocation structures. The quasi homogeneous lath structure, formed by quenching, is disrupted by plastic deformation producing a composite structure. Lath packets oriented favorably or unfavorably for dislocation glide become soft or hard. Two lath packet types develop by work softening or work hardening in which the dislocation densities become smaller or larger compared to the initial average dislocation density. The decomposition into soft and hard lath packets is accompanied by load redistribution and the formation of long-range internal stresses between the two lath packet types. The composite behavior of plastically deformed lath martensite opens a new way to understand the elastic-plastic response in this class of materials.

Keywords: *composite behavior of lath martensite, elastic-plastic response of lath martensite, neutron diffraction line profile analysis, characteristically asymmetric peak profiles, role of mean free path of dislocations*

[&]*Corresponding author: ungar@ludens.elte.hu*

1. Introduction

Lath martensitic steels are widely used iron base alloys with outstanding mechanical properties. They contain carbon varying between a few hundredths to a few tenths of weight percentage and a variety of different alloying elements in small quantities. Their strength is induced by the transformation of the fcc γ to the bcc α phase by fast cooling [1]. Coherency strains in the quenched alloy induce huge dislocation densities which are the source of the alloy's strength [1]. Though this alloy has been used since the existence of steel, the way its microstructure functions is still unclarified.

A typical lath-martensite consists of blocks of lamellar plates, where the blocks form packets [2-4]. The blocks are subdivided into sub-blocks, where the smallest constituents are lamellar plates called martensite-laths. The hierarchy of packets, blocks, sub-blocks and laths is shown schematically in Fig. 1. Within the packets the laths are parallel lamellae each having crystal orientations separated by different twin-related boundaries. The 110 oriented lath planes align coherently with one of the 111 type planes of the primary austenite. Within the primary austenite grain boundary, several packets of different crystallographic orientations can coexist [2-4], see Fig. 1a.

Despite the rather large yield stress of martensitic steels, they do show some ductility [1,5-7]. Recent microscale deformation experiments [8,9] have attempted to reveal the microscopic mechanisms controlling plastic deformation in lath-martensite. Micropillars with a single martensite block have shown perfectly ideal stress-strain behavior with no strain hardening and a flow stress of ~1.2 GPa. Micropillars with two or more blocks, however, have shown significant strain hardening with a similarly large yield stress [8]. Microscale tensile experiments have shown relatively small flow-stress values of the order of ~350 MPa, when the active slip systems were in-lath-plane, whereas the flow-stress almost doubled when the active slip systems were out-of-lath-plane [9]. The two experiments in [8] and [9] indicated that there might be a load redistribution between packets in which the active slip systems are in- or out-of-lath-plane, respectively. This is shown schematically in Fig. 1b, where we can see two packets oriented with active Burgers vectors either in- or out-of-lath-plane.

T present work is based on characteristically asymmetric neutron diffraction profiles. We will show for the first time that although the microstructures of lath packets in lath-martensitic steels are similar in the as-quenched initial state, this homogeneity is disrupted during plastic deformation. The disruption is the result of the process where lath-packets with active Burgers vectors in-lath-plane work-soften, whereas those with active Burgers vectors out-of-lath-plane work-harden. Plastic deformation produces coexisting soft and hard lath packets, and the deformed lath martensite behaves like a composite. The composite behavior could be regarded as a new paradigm allowing us to understand the elastic-plastic response of lath martensite

2. Experimental

An as-quenched rod-shape lath martensite steel specimen was tensile deformed in a screw-type loading machine at a strain rate of 10^{-5} s^{-1}. Strain was measured by a strain gauge glued on the specimen. The composition of the specimen was Fe-0.22C-0.87Si-1.64Mn-0.024Ti-0.0015B-0.0025N (all in wt.%). The as quenched martensitic steel specimen contained a small amount of retained austenite of the order of about 3%. Scanning electron microscopy (SEM) images revealed no significant texture. According to the SEM micrographs the average packet and block sizes were about 20 and 4 μm, respectively. Further details of the specimen will be given in [10].

The experiments took place at the TAKUMI beamline of the Materials and Life Science Experimental Facility of the Japan Proton Accelerator Research Complex, J-PARC. The tensile machine was placed into the TAKUMI beamline and the neutron diffraction patterns were collected in-situ during the tensile deformation. The beamline was operated in the high resolution and high intensity time-of-flight (TOF) mode. High resolution was achieved by tuning the incident optical devices, especially the neutron guides and collimators, for this purpose. Despite the loss of intensity, due to high resolution, high intensity was retained since the instrument was built at a pulsed, high intensity spallation-neutron-source. The schematic outline of the TOF diffractometer and the specimen geometry are shown in Fig. 2 and will be discussed in more detail in [10]. The illuminated volume in the specimen was restricted to $5\times5\times5$ mm^3 by the incident beam slit and the radial collimators. The instrumental peak width was tuned to 0.3 %.

The loading direction and the diffraction vectors were either parallel or perpendicular to each other regarding the +90° or the -90° detectors, i.e. in the 'axial' or the 'side' cases, respectively, as indicated in Fig. 2. The intrinsic peak asymmetry due to TOF geometry in the TAKUMI diffractometer produces slightly longer profile tails in the larger d value directions. This effect, however, will be neglected, since it is significantly smaller than the asymmetry caused by the long range internal stresses in the specimen. Details follow in the next paragraph.

Strains or stresses, which are related to directions normal to the tensile direction, are often called radial strains or stresses. In the present work we will call these side-case strains or stresses, since the same terms were used in earlier literature on long range internal stresses, see Refs. [11-13].

3. Evaluation of asymmetric peak profiles in terms of local dislocation densities and long-range-internal-stresses

In order to improve the counting statistics, the deformation was interrupted at 9 consecutive strain values as shown in the stress-strain curve (see Fig. 3). Line profile analysis has been done on the diffraction patterns measured in the unloaded states of the specimen. These diffraction patterns were evaluated by the Convolutional-Multiple-Whole-Profile (CMWP) fitting procedure based on physically modelled profile functions for dislocations, crystallite size and planar defects [14,15]. The size profile function, I^S, is constructed by assuming a logarithmic-normal size distribution of the coherently scattering domains. The size distribution function is described by the median, m, and its variance, ζ. The strain profile, I^D, is based on dislocations characterized by the average density, ρ, and the arrangement parameter, M, where $M=R_e\sqrt{\rho}$ and R_e is the effective outer cut-of radius of dislocations. When the dislocation arrangement has a strong dipole character, i.e. when their strain field is strongly screened, R_e will be smaller than the average dislocation distance and M becomes smaller than 1 ($M\leq1$). When, however, the dislocation arrangement has a weak dipole character, i.e. when the strain field is weakly screened, R_e will be larger than the average dislocation distance and M becomes larger than 1 ($M\rangle\rangle1$). Strain broadening is also anisotropic as a function of reflection order, or the *hkl* indexes. This effect is caused by elastic anisotropy of the material. Strain anisotropy is taken into account by the contrast factors, C, of the different *hkl* diffraction profiles. When the texture is not strong and the possible slip systems are randomly populated by dislocations, the contrast factors can be averaged over the permutations of the *hkl* indexes. In such cubic polycrystalline materials the average contrast factors are a function of a single parameter, $\bar{C} = \bar{C}(q)$.

In the present martensitic alloy there are no planar defects, therefore we have described line broadening only by the size effect and dislocations. The size and strain profile functions are given by m, ζ, ρ, M and q. The asymmetric profiles require two size and two strain profiles. This means that the microstructure has been characterized by altogether 10 physical parameters. In order to improve the reliability of the evaluation, the CMWP software package has recently been amended [16]. The global minimum of the physical parameters is obtained by combining the Marquard-Levenberg nonlinear least-squares method and the Monte-Carlo fitting procedure [16]. The improved CMWP applies the two procedures alternatingly, while, in the Monte-Carlo procedure, the relative searching range of the physical parameters decreases exponentially form about 0.4 to about 0.02. The quality of the fit has been measured by the goodness-of-fit, R^2, value. The CMWP evaluation was carried out for all diffraction peaks from 110 to 330 simultaneously. A typical axial diffraction pattern for the ε=0.03 tensile deformed state is shown in Fig. 4a.

To describe the strain part of asymmetric profiles we used the sum of two symmetric strain profile functions, each of which were shifted to smaller or larger d* values around the center of gravity of the measured peaks. The robustness of the fitting procedure is shown in Fig. 4b. In order to see the difference between fitting with a single or two strain profiles only a section of the pattern is shown between d*=6.5 nm and d*=11.7 nm. Asymmetry concerns mainly the lower intensity parts of the profiles. In order to see the quality of fitting better, the intensity is in logarithmic scale. In the upper pattern two, whereas in the lower pattern only one strain profile has been used. In the upper measured (open circles) and fitted (red solid line) patterns the fitting is very good on both sides of the asymmetric profiles. Here R^2=0.9045 has been obtained. In the lower measured (open circles) and fitted (red solid line) patterns the fitting is good on the right hand side, however, on the left hand side, especially in the lower intensity ranges, the measured data are well above the fitted curves indicating that the second peak is missing. Here R^2 has been obtained to be R^2=0.782.

In the initial state, all the diffraction peaks are almost perfectly symmetric within the experimental error. However, in the tensile deformed states, they become pronouncedly asymmetric, beyond the experimental error. This is illustrated for the 200 axial and side case diffraction peaks in Figs. 5a and 5b, respectively. The figures clearly show that after deformation the peaks become asymmetric and that the asymmetries in the axial and side case peaks occur in opposite directions. The tail parts of the asymmetric peaks are longer in the smaller or the larger d* directions in the axial or side cases, respectively. Here d*=1/d, the reciprocal of the d spacings in the crystal. The reversal of peak asymmetry is qualitatively similar to the characteristic peak asymmetry observed earlier in tensile deformed copper single [11-13] or polycrystals [17-20] with dislocation cell structures. This type of peak asymmetry is evidence for the composite behavior in heterogeneous microstructures, especially in heterogeneous dislocation distributions.

The evaluation of the sub-peak shifts, Δd^*, is shown in Fig. 5c and 5d for two typical 200 axial and side case profiles. The *hkl* dependent local strains, $\varepsilon_{hkl}=(\Delta d/d)_{hkl}$, have been evaluated from the sub-peak shifts, Δd^*, and are shown for the 200, 211, 220 and 310 reflections in Fig. 6a as a function of true strain. The figure indicates that the absolute values of ε_{hkl} for the 200 and 310 reflections are systematically larger than the shifts of the 211 and 220 sub-peaks. This effect is due to elastic anisotropy. The *hkl* dependent local long-range internal stresses, $\Delta\sigma_{hkl}$, have been calculated as: $\Delta\sigma_{hkl}=E_{hkl}\Delta\varepsilon_{hkl}$, where E_{hkl} are the *hkl* dependent Young's modules. The E_{hkl} values have been determined in [10] from the elastic parts of the lattice strain measurements for the same specimen investigated here also. The measured values are: E_{100}=167(±2) GPa, E_{110}=229(±3) GPa, E_{211}=223(±3) GPa and E_{310}=183(±3) GPa. The $\Delta\sigma_{hkl}$ values are plotted as a function of the true stress in Fig. 6b. The figure indicates that these values reveal a much weaker *hkl* dependence than the ε_{hkl} values. This result suggests that the behavior of the long-range internal stresses conforms more to the Taylor [20] than to the Sachs [21] model of plasticity. Both, ε_{hkl} and $\Delta\sigma_{hkl}$ have been evaluated also from the asymmetric side-case profiles. The values were obtained to be smaller than from the axial-case profiles by a factor of Poisson's number, i.e by about a factor of 0.33.

The two shifted sub-profiles have been evaluated for the average dislocation densities in the HO and SO packet components. The results are shown as a function of strain in Fig. 7a. The integral intensity ratio of the sub-profiles corresponding to the HO and SO packets provided the volume fractions of the two components, f_{HO} and f_{SO}. We will denote the stresses acting in the tensile and shear directions by σ and τ. The two stresses are coupled by the Taylor factor, M_T: $\sigma=M_T\tau$ [20]. The average flow stress values, σ_{av} or τ_{av}, and the local flow stress values, σ_{HO} or τ_{HO} and σ_{SO} or τ_{SO}, acting in the HO and SO packets, have been calculated by the Taylor equation [23]:

$$\sigma_i = \sigma_0 + \alpha G M_T b\sqrt{\rho_i}\,, \qquad (1a)$$

$$\tau_i = \tau_0 + \alpha G b\sqrt{\rho_i}\,, \qquad (1b)$$

where i stands for, HO or SO, α is a free parameter usually between zero and 1, G is the shear modulus, b is the absolute value of the Burgers vector and ρ_i is the total or the local average dislocation density, latter either in the hard, HO, or soft, SO, packets, respectively. Throughout this work all local parameter values are average values for all the grains within the illuminated volume of the polycrystalline specimen. Rietveld refinement has been done allowing for the two phases, i.e. the HO and SO fractions of the packets. The details of this analysis are given in [10]. Rietveld analysis did provide the same average lattice parameter values for the two components as the ones one could obtain from the peak shifts determined here.

4. Evolution of the dislocation density and structure in HO and SO martensite lath-packets

During plastic deformation, dislocations are created and annihilated at the rates of creation, $\dot{\rho}_{cr}$, and annihilation, $\dot{\rho}_{anni}$. In work hardening the creation rate exceeds the annihilation rate, $\dot{\rho}_{cr} > \dot{\rho}_{anni}$, and the total dislocation density increases, $\dot{\rho}_{tot} > 0$. At large deformations the rate of annihilation can increase to match the rate of creation, $\dot{\rho}_{cr} = \dot{\rho}_{anni}$, and the total dislocation density will reach a saturation value, $\rho_{tot}=\rho_{sat}$, where $\dot{\rho}_{tot} = 0$. In Ref. [24] it was shown that if, for any reason, the starting dislocation density is larger than the saturation value, i.e. $\rho_{ini}>\rho_{sat}$, the annihilation rate will exceed the rate of creation, $\dot{\rho}_{anni} > \dot{\rho}_{cr}$. Under these conditions the total dislocation density will decrease even during plastic deformation, $\dot{\rho}_{tot} < 0$. In such a case work softening can be observed.

In lath martensites the initial dislocation density, ρ_{ini}, is created by martensitic transformation. The process produces very large dislocation densities of the order of 10^{16} m^{-2} [3,25]. In Ref. [24] it was shown that work hardening or softening depends on the relation between the initial, ρ_{ini}, and the saturation values, ρ_{sat}, of the dislocation densities. The two processes are uniformly described by equation (6) in Ref. [24]:

$$\rho(\gamma) = [(\rho_{sat})^{1/2} - \beta\, exp(-\frac{y*\gamma}{2b})]^2 , \qquad (2)$$

where γ is the shear deformation, $\beta=(\sqrt{\rho_{sat}} - \sqrt{\rho_{ini}})$, y* is the effective annihilation distance of dislocations as defined in Refs. [24], [26] and [27] and $\gamma=2\varepsilon$, ε being the deformation in the tensile direction. We shall interpret only the ratio of the annihilation distance in the soft and hard components of the deformed lath-martensite, y^*_{SO}/y^*_{HO}. The interpretation of the annihilation distance, y* itself, is not an essential issue, since in equation (2) it is only a fitting parameter. Based on the Orowan equation [28] it can be assumed that the mean free path of dislocations, Λ, scales with the average dislocation distance, $\Lambda=h'/\sqrt{\rho}$, where h' is the scaling factor. In Refs. [26,27] it was shown that at saturation the annihilation distance also scales with the saturation value of the dislocation distance: $y^*= h''/\sqrt{\rho_{sat}}$, where h'' is the scaling factor. Since both, y* and Λ_{sat} scale with $1/\sqrt{\rho_{sat}}$, the ratios of the two quantities in the SO and HO components of the deformed lath martensite are equal at saturation:

$$y^*_{SO}/y^*_{HO} = \Lambda^{SO}_{sat}/\Lambda^{HO}_{sat} \cong 50\ . \qquad (3)$$

The dislocation density values at saturation, ρ_{sat} and the signed values of β in the SO and HO components, as obtained from equation (2), are listed in Table 1. When β is positive or negative, the rate of dislocation annihilation is smaller or larger than the rate of dislocation creation, respectively [24]. The former case corresponds to work hardening and the latter to work softening.

In the packets where the active dislocations (i.e. the dislocations with the largest Schmid factor) move along the lath planes, the mean free paths, Λ, and the effective annihilation distances, y*, will be relatively long. When, however, the active dislocations cross the lath-plane boundaries both the mean free paths, Λ, and the effective annihilation distances, y*, will be relatively short. In the first case, the lath-packets will soften, whereas in the second case they will harden, producing soft and hard packets with composite behavior. Softening and hardening disrupts the dislocation distribution which was homogeneous on the scale of lath dimensions in the as quenched initial state. In the SO and HO components the dislocation densities decrease or increase relative to the initial average value, and vary spatially on the length scale of martensite packets. Load is redistributed between SO and HO martensite packets in correlation with the composite behavior. Dislocation dynamics simulations in fcc crystals, see Ref. [29], have shown that the mean free path of dislocations play a key role in strain hardening. The present work indicates that Λ along with y* are key quantities in strain softening or hardening, which is in good correlation with [29].

Screw or edge type dislocations have different diffraction contrast [30]. The CMWP procedure takes into account strain anisotropy and also provides the average fraction values of edge and screw type dislocations [14,15]. The analysis provided that in the SO packets the dislocations are mainly of screw character, which does not change during plastic deformation. In the HO components, however, the dislocation character changes gradually from screw to edge character as a function of plastic strain, as indicated in Table 1. Screw dislocations can move in any direction therefore annihilate relatively easily even when they are farther apart from each other. Edge dislocations, however, will either glide on slip planes or climb when annihilating, so can only annihilate when they are close to each other. The relatively large ratios between the effective annihilation distances and mean free paths in the SO and HO packets, see in eq. (3), correlate well with the different dislocation characters in these packets. Further details on how dislocation character changes with plastic deformation will be given in Ref. [10].

The total average dislocation density, ρ_t, was calculated from the two local values as the weighted average, $\rho_t = f_{HO}\rho_{HO} + (1 - f_{HO})\rho_{SO}$, where f_{HO} is the volume fraction of the HO component. The volume fraction, f, of the HO fraction has been found to vary around f=0.48±0.05, right from the beginning of plastic deformation and it did not change within the investigated deformation range. The flow stress values, σ_i, calculated by equation (1) are shown in Fig. 7b *vs*. the measured applied stress, $\sigma_{applied}$. In equation (1), α was allowed to vary with deformation in the HO oriented packets as it is shown in Fig. 7c.

The value of α is usually considered a constant, but in the HO packets we must have an α with a changing value. Unless we have a changing α value, the increase of dislocation density alone would be totally insufficient to account for the increase in the flow stress. A number of experimental results have shown that the value of α changes with dislocation arrangements during plastic deformation [31-35]. In the SO packets the dislocation density decreases at the beginning of plastic deformation and then stays constant. Since here neither the dislocation density nor its arrangement changes considerably, the value of α is a constant. The local flow stresses, σ_{HO} and σ_{SO} in the HO and SO packets indicate that the moment plastic deformation starts, stress is redistributed between the two packet types, see Fig. 7b. Compared to the applied stress values, the local flow stress decreases in the SO packets, but increases in the HO packets. The $\sigma_{initial}$ value is the flow stress corresponding to the initial average dislocation density: $\sigma_{initial}=\sigma_0+\alpha G M_T b\sqrt{\rho_{initial}}$, where σ_0 is the friction stress of the alloy.

5. Composite model of plastically deformed lath-martensite

The shifts, Δd^*, are evaluated in terms of residual internal stresses, $\Delta\sigma$, corresponding to the forward and backward stresses which act in the hard-orientation (HO) or soft-orientation (SO) packets. The two different packet orientations, HO and SO, are those in which the active Burgers vectors are out-of-lath-plane and in-lath-plane.

The microscopic model of stress redistribution is based on the composite model of Mughrabi [11-13] and is shown schematically in Fig. 8. In the initial state, the microstructures are identical in the packets with different orientations. Fig. 8a shows three adjacent packets with identical dislocation structures. Two packets have vertical and one has horizontal laths. In the central packet the active Burgers vector is parallel to the lath plane directions, whereas in the other two they cross the lath boundaries. As schematically shown in Fig. 8b, the central SO packet will soften during plastic deformation whereas the HO packets will harden. After unloading, forward and backward residual stresses will remain in the HO and SO packets, respectively. Stress and strain compatibility between the SO and HO packets is guaranteed by the geometrically necessary dislocations (GNDs). They are lined up along the interfaces of the differently oriented packets shown in Fig. 8c. The forward and backward local residual stresses are shown in Fig. 8d. During loading the weighted averages of the local stresses add up to the applied stress [11]:

$$\tau_{applied} = f_{HO}\tau_{HO} + (1-f_{HO})\tau_{SO} . \quad (4)$$

After unloading the residual internal stresses in the HO and SO packets are:

$$\Delta\tau_{HO}=\tau_{HO}-\tau_{applied}\ ,\ \ \Delta\tau_{SO}=\tau_{SO}-\tau_{applied}\ ,\ \text{where}\ \ f_{HO}\Delta\tau_{HO} + (1-f_{HO})\Delta\tau_{SO} = 0. \qquad (5)$$

In the composite model of plastic deformation of heterogeneous microstructures, $\Delta\tau_{HO}$ and $\Delta\tau_{SO}$ are called 'long range internal stresses' [11-13]. During plastic deformation, the backward stresses in the SO and the forward stresses in the HO packets will either hamper or assist dislocation motion so as to make the entire material flow simultaneously. The backward and forward stresses ensure that macroscopic flow takes place irrespective of the packets being soft or hard. In the HO packets the dislocation character gradually changes from screw to edge type when plastic deformation takes place. This change in dislocation character causes the annihilation distance to decrease, which in turn contributes to the increase of dislocation density. Statistical fluctuations are not taken into account in the simple schematic model of long range internal stresses, see Fig. 8d. No doubt the magnitude of long range internal stresses varies statistically as has been shown in several high resolution X-ray diffraction experiments [17-20]. The local variation and fine details of the long range internal stresses requires similar high resolution X-ray diffraction experiments as in the case of plastically deformed copper crystals [17-20]. The strengthening effect of retained austenite has not been discussed here, but further details will be given in [10]. In the present alloy the volume fraction of retained austenite is about 3.7%. As it will be discussed in [10], this amount contributes to the average strength of the material. However, the contribution is less than about 9%, and has practically no effect on the long range internal stresses or the composite behavior described and discussed here.

Conclusions

Based on high-resolution neutron diffraction experiments we have shown that the initially homogeneous dislocation structure in lath-martensite is disrupted by tensile deformation. Packets with active Burgers vectors having either in-lath-plane or out-of-lath-plane orientation, will soften or harden as a function of plastic deformation. The dislocation densities will become smaller or larger than the initial average value in the softening or hardening packets. Plastic deformation produces a heterogeneous microstructure consisting of soft and hard martensite packets, and the material, thus consisting of two components, behaves like a composite. Long range internal stresses are being formed, and they act backward or forward in the soft and hard components. Load is redistributed between the soft and hard components. The backward and forward stresses hamper or assist dislocation movement in the soft or hard components. As a result, both components undergo plastic deformation simultaneously. In order to understand the relatively ductile and high strength nature of lath-martensite steels, one has to take into account that the initially homogeneous microstructure will turn into a composite as a result of plastic deformation.

Acknowledgements

The authors are grateful to the Japan Society for the Promotion of Science Grant-in-Aid for Scientific Research for partial support under grant No. 26289264. T.U. and G.R are grateful for the partial support of the French State through the program "Investment in the future" operated by the National Research Agency (ANR) and referenced by ANR-11-LABX-0008-01, LabEx-DAMAS. The authors thank the Education Commission of Hubei Province of China (No. B20161203), for the specimen. The neutron diffraction experiments were conducted at the Materials and Life Science Experimental Facility of J-PARC with the proposals of 201410019.

References

1. G. Krauss, *Mater. Sci. Eng*., 1999, vol. A273–275, pp. 40-57.
2. G. Krauss, A. R. Mader, *Metallurgical Transactions*., 1971, vol. 2, pp. 2343-2357.
3. S. Morito, H. Tanaka, R. Konishi, T. Furuhara, T. Maki, *Acta Mater*., 2003, 51, pp. 1789-1799.
4. H. Kitahara, R. Ueji, N. Tsuji, Y. Minamino, *Acta Mater*., 2006, vol. 54, pp. 1279–1288.
5. T. Swarr, G. Krauss, *Metall. Transact*., 1976, vol. 7A, pp. 41-48.
6. M. Michiuchi, S. Nambu, Y. Ishimoto, J. Inoue, T. Koseki, *Acta Mater*., 2009, vol. 57, pp. 5283-5291.
7. S. Nambu, M. Michiuchi, Y. Ishimoto, K. Asakura, J. Inoue, T. Koseki, *Scripta Mater*., 2009, vol. 60, pp. 221–224.
8. H. Ghassemi-Armaki, P. Chen, S. Bhat, S. Sadagopan, S. Kumar, A. Bower, Acta Mater. 61 (2013) 640–3652.
9. Y. Mine, K. Hirashita, H. Takashima, M. Matsuda, K. Takashima, *Mater. Sci. Eng*., 2013, vol. A560, pp. 535–544.
10. S. Harjo, T. Kawasaki, Y. Tomota, W. Gong, K. Aizawa, Z. Shi, G. Ribárik, T. Ungár, to be submitted to Int. J. Plasticity.
11. H. Mughrabi, *Acta Metall*., 1983, vol. 31, pp. 1367-1379.
12. T. Ungár, H. Mughrabi, D. Rönnpagel, M. Wilkens, *Acta Metall*., 1984, vol. 32, pp. 333-342.
13. H. Mughrabi, T. Ungár, W. Kienle, M. Wilkens, *Philos. Mag*., 1986, vol. A53, pp. 793-813.
14. G. Ribárik, T. Ungár, *Mater. Sci. Eng*., 2010, vol. A528, pp. 112–121.
15. T. Ungár, L. Balogh, G. Ribárik, *Metall. Mater. Trans*., 2010, vol. A41, pp. 1202-1209.
16. G. Ribárik, B. Jóni, T. Ungár, *in preparation*.
17. B. Jakobsen, H. F. Poulsen, U. Lienert, J. Almer, S, D. Shastri, H. O. Sørensen, C. Gundlach, W. Pantleon, *Science*, 2006, vol. 312, pp. 889–892.
18. L. E. Levine, B. C. Larson, W. Yang, M. E. Kassner, J. Z. Tischler, M. A. Delos-Reyes, R. J. Fields, W. Liu, *Nature Materials*, 2006, vol. 5, pp. 619–622.
19. H. Mughrabi, T. Ungár, *Nature Materials*, 2006, vol. 5, pp. 601–602.

20. B. Jakobsen, H. F. Poulsen, U. Lienert, W. Pantleon, *Acta Mater*., 2007, vol. 55, pp. 3421-3430.
21. G. I. Taylor, *J. Inst. Metals*, 1938, vol. 62, pp. 307-324.
22. G. Sachs, (1928). Zeitschr. Verh. Deutsch. Ing., 1928, vol. 72, 734-736.
23. G. I. Taylor, *Proc. R. Soc. Lond*., 1934, vol. A145, pp. 362-387.
24. T. Ungár, L. Li, G. Tichy, W. Pantleon, H. Choo, P. K. Liaw, *Scripta Mater*., 2011, vol. 64, pp. 876-879.
25. K. Nakashima, Y. Fujimora, H. Matsubayashi, T. Tsuchiyama, S. Takaki, *Tetsu-to-Hagane (in Japanese)*, 2007, vol. 93, pp. 459-465.
26. U. Essmann, M. Rapp, *Acta Metall*., 1973, vol. 21, pp. 1305.
27. U. Essmann, H. Mughrabi, *Philos. Mag*., 1979, vol. 40, pp. 731-756.
28. E. Orowan, *J. West Scotland. Iron Steel Inst*., 1946, vol. 54, pp. 45-53.
29. B. Devincre, T. Hoc, L. Kubin, *Science*, 2008, vol. 320, pp. 1745-1748.
30. M. Wilkens, *phys. stat. sol. (a)*, 1970, vol. 2, pp. 359-370.
31. H. Mughrabi, *Mater. Sci. Eng*., 1987, vol. A85, pp. 15-31.
32. E. Schafler, K. Simon, S. Bernstorff, P. Hanák G. Tichy, T. Ungár, M. J. Zehetbauer, *Acta Mater*., 2005, vol. 53, pp. 315-322.
33. T. Ungár, A. D. Stoica, G. Tichy, X.-L. Wang, *Acta Mater*., 2014 , vol. 66 pp. 251-261.
34. H. Mughrabi, *Current Opinions Sol. State Mater. Sci*. 2016, in the press.
35. B. P. J. Sandvik, C. M. Wayman, *Metall. Transac*., 1983, vol. A14, pp. 809-822.

Table 1. The dislocation density values at saturation, ρ_{sat} as provided by equation (2), the signed values of β in the soft and hard components of the deformed lath martensite, as defined in equation (2) and the dislocation character of the majority of dislocations at saturation as provided by the CMWP procedure.

packets	ρ_{sat} [10^{15} m^{-2}]	β [1/nm]	dislocation character at saturation
SO	1.69 (±0.1)	-0.71 (±0.05)	screw
HO	18.7 (±1)	2.27 (±0.2)	edge

Captions

Figure 1.
Schematic illustration of the hierarchical structure of lath martensite with the active Burgers vectors. (a) Lath packets consisting of parallel blocks in three different packet. Each block consists of laths of two specific Kurdumov–Sachs [2] variant groups (sub-blocks) misoriented by small angles smaller than about 10 degrees. (b) Two packets oriented with the active Burgers vectors either in- or out-of-lath-plane relative to the direction of the applied stress, σ, respectively.

Figure 2.
Schematic drawing of the in-situ neutron diffraction experiment. The specimen was mounted horizontally in a loading machine which was installed at the TAKUMI beamline, in such a way that the neutron diffraction patterns in the axial and axial directions were measured simultaneously using two detector banks at scattering angles of ±90°.

Figure 3.
Stress-strain curve. Deformations in plastic regime were increased step by step followed by unloading at several strain values to improve counting statistics.

Figure 4.
(a) Typical diffraction pattern. The observed (open black-circles) and CMWP fitted (red line) neutron diffraction patterns for the $\varepsilon = 0.03$ tensile deformed state. The horizontal axis is the reciprocal of the d spacings, where $d^*=1/d$. (b) A section of the measured (open black-circles) and CMWP fitted (red line) patterns. The upper patterns: with fitting two slightly shifted strain profiles into each peak profile in order to account for peak asymmetries. The lower patterns: with only one fitted strain profile into each peak profile. The letter A at the *hkl* indices indicates austenite reflections.

Figure 5.

Enlarged 200 diffraction profiles. The measured and CMWP calculated profiles for the undeformed (open triangles and blue lines) and $\varepsilon = 0.047$ tensile deformed (open squares and red lines) states in the axial (a) and axial (b) directions. (c) The CMWP calculated sub-profiles corresponding to the HO (dark green line) and the SO (blue line) packets in the axial direction, along with the measured data (open circles) and the CMWP calculated total profile (red line). The center of gravity of the measured profile and the positions of the sub-peaks are indicated as dotted, dashed and dash-dot lines, respectively. (d) The measured (open circle), the CMWP calculated total profile (red line) and the CMWP calculated sub-profiles corresponding to the HO (dark green line) and the SO (blue line) packets in the axial direction.

Figure 6.

(a) The relative shifts, $\Delta d/d$, of the sub-peaks obtained from the asymmetric axial case profiles as a function of true strain for the 200, 220, 311 and 222 reflections. (b) The long-range internal stress values, $\Delta\sigma$, as a function of trues train for the 200, 220, 311 and 222 reflections. The vertical thick black lines indicate the experimental error.

Figure 7.

Dislocation density, stress partitioning and α parameter in the Taylor equation. (a) Dislocation densities in the HO (red symbols) and the SO packets (blue symbols), and the volume fraction weighted average dislocation densities (black symbols). (b) Local stresses in the HO (red symbols) and the SO packets (blue symbols) calculated from the dislocation densities according to the Taylor equation in eq. (1). (c) The α parameter in Taylor's equation calculated from the dislocation densities and the local stresses.

Figure 8.

Schematic drawing of the composite model of the SO and HO packets in lath martensite. (a) Schematic arrangement of laths in different packets. The parallel laths are indicated by different parallel gray-scales. (b) Active Burgers vectors relative to the direction of the shear stress, τ, in the HO and SO packets. (c) Schematic illustration of the GNDs lined up along the interfaces of the differently oriented packets. (d) Spatial distribution of the local long-range-internal-stresses in the HO and SO packets under the action of the applied stress.

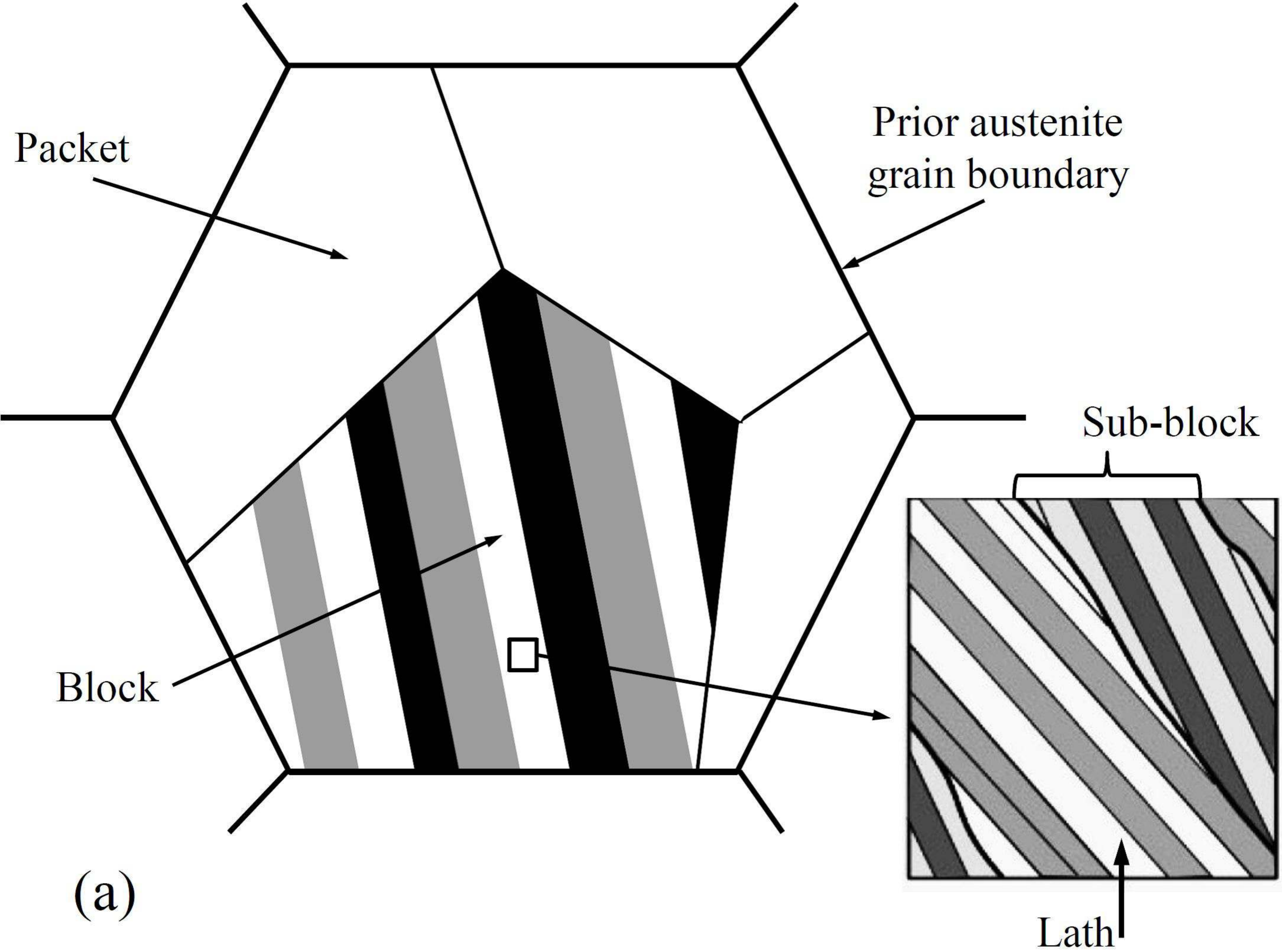
Prior austenite
grain boundary
Packet
Sub-block
Block
Lath
(a)

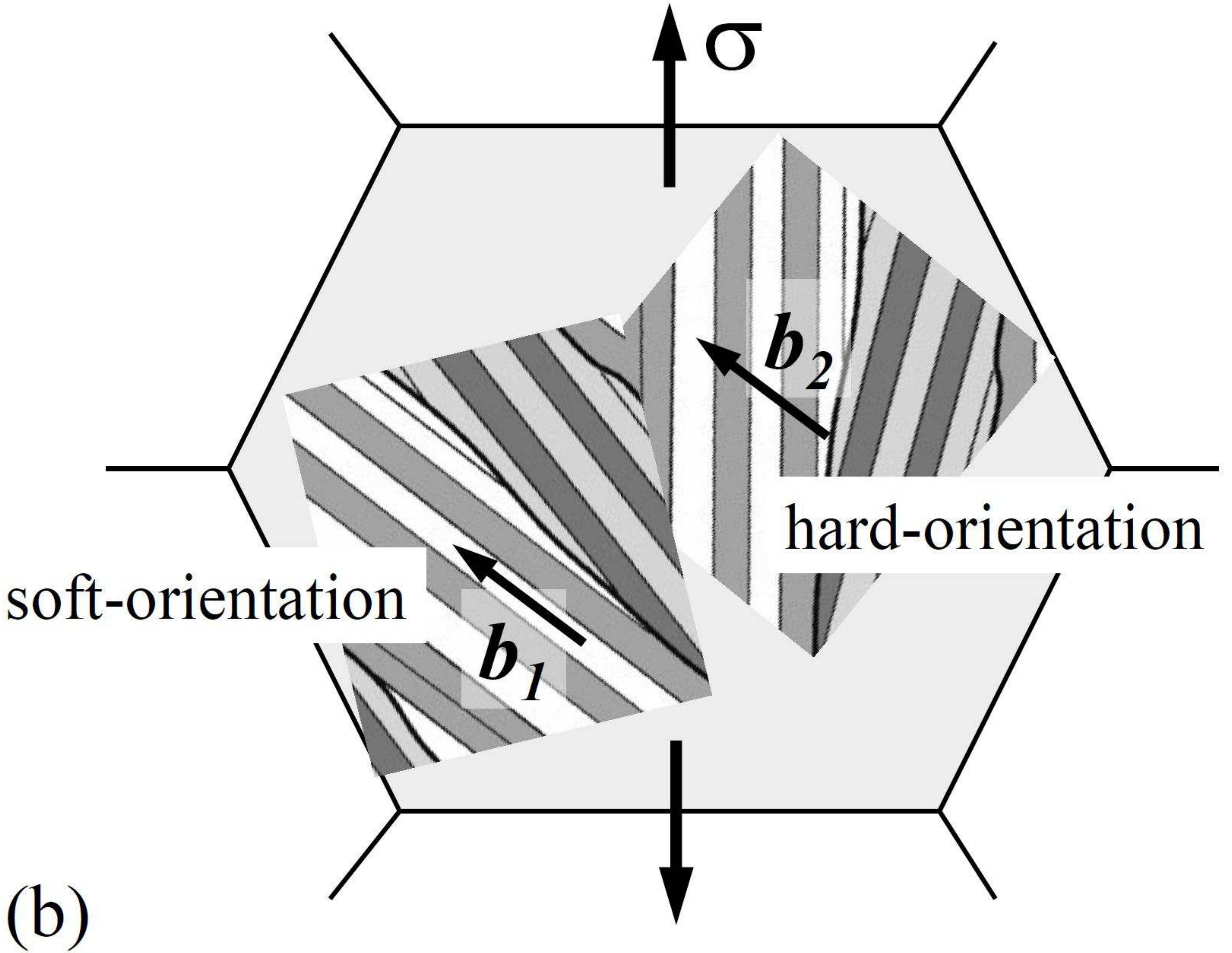

σ
b_2
hard-orientation
soft-orientation
b_1
(b)

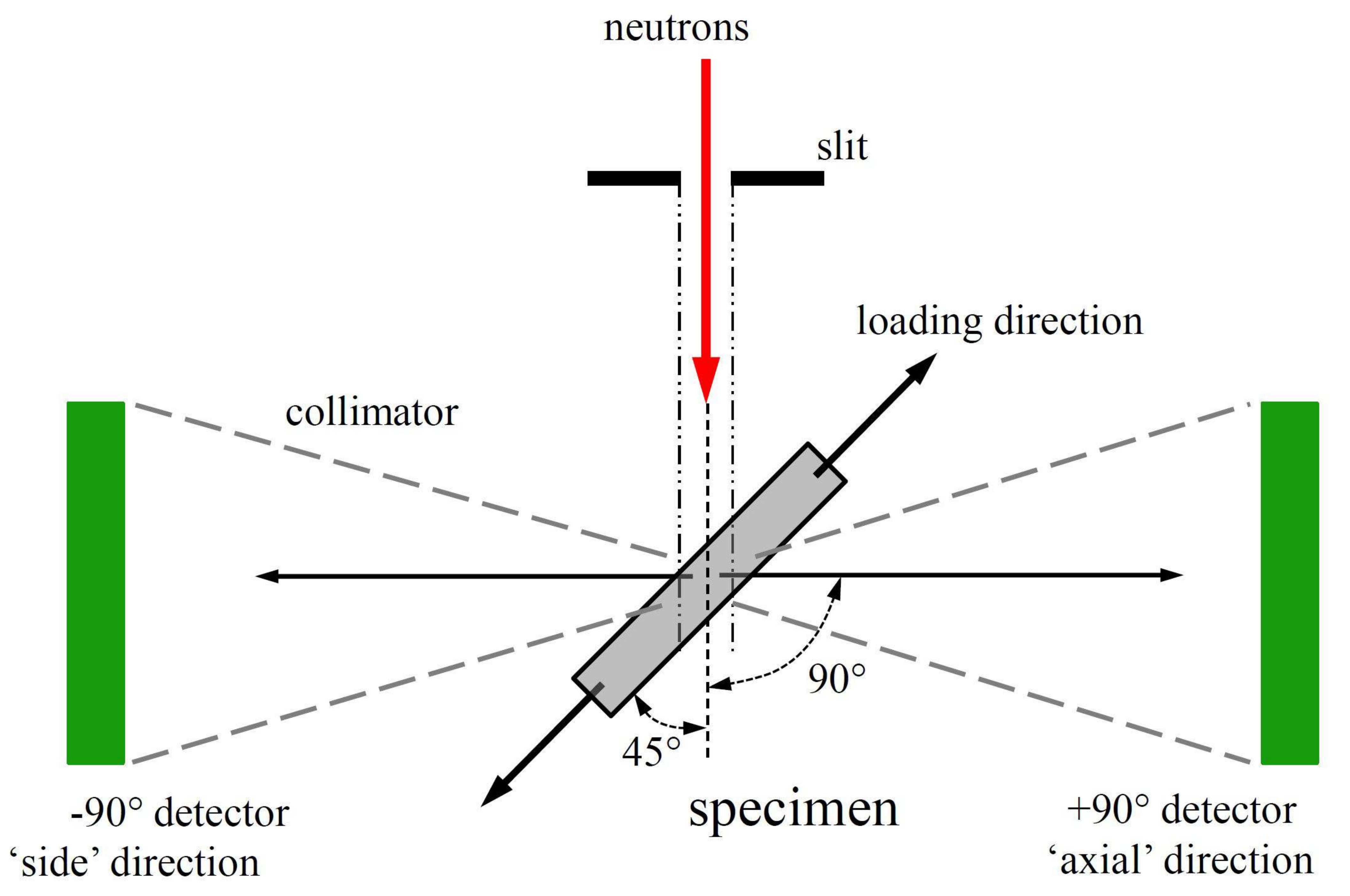
neutrons
slit
loading direction
collimator
90°
45°
-90° detector
'side' direction
specimen
+90° detector
'axial' direction

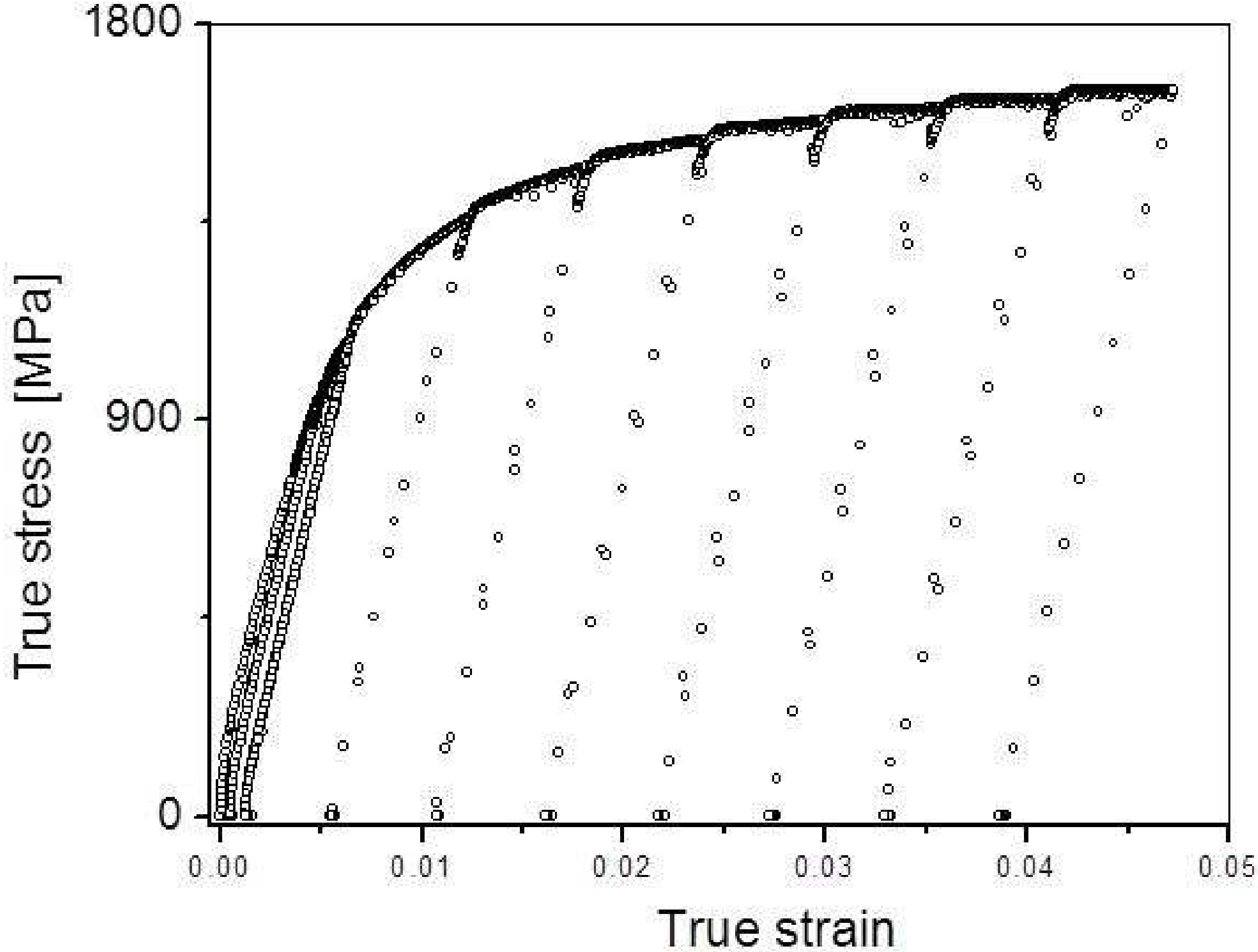

1800
900
0
True stress [MPa]
0.00
0.01
0.02
0.03
0.04
0.05
True strain

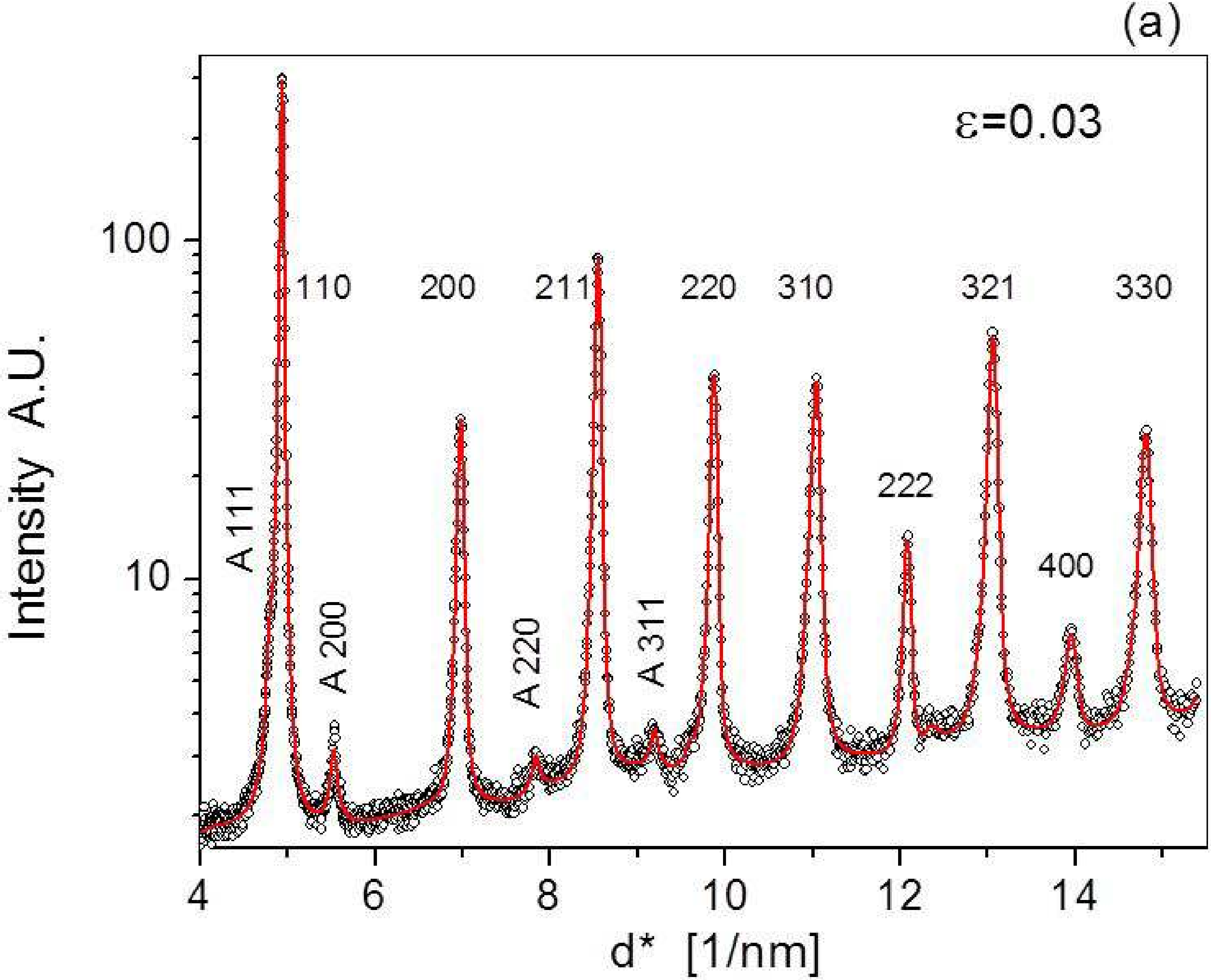

(a)
ε=0.03
Intensity A.U.
100
10
110
200
211
220
310
321
330
222
400
A 111
A 200
A 220
A 311
4
6
8
10
12
14
d* [1/nm]

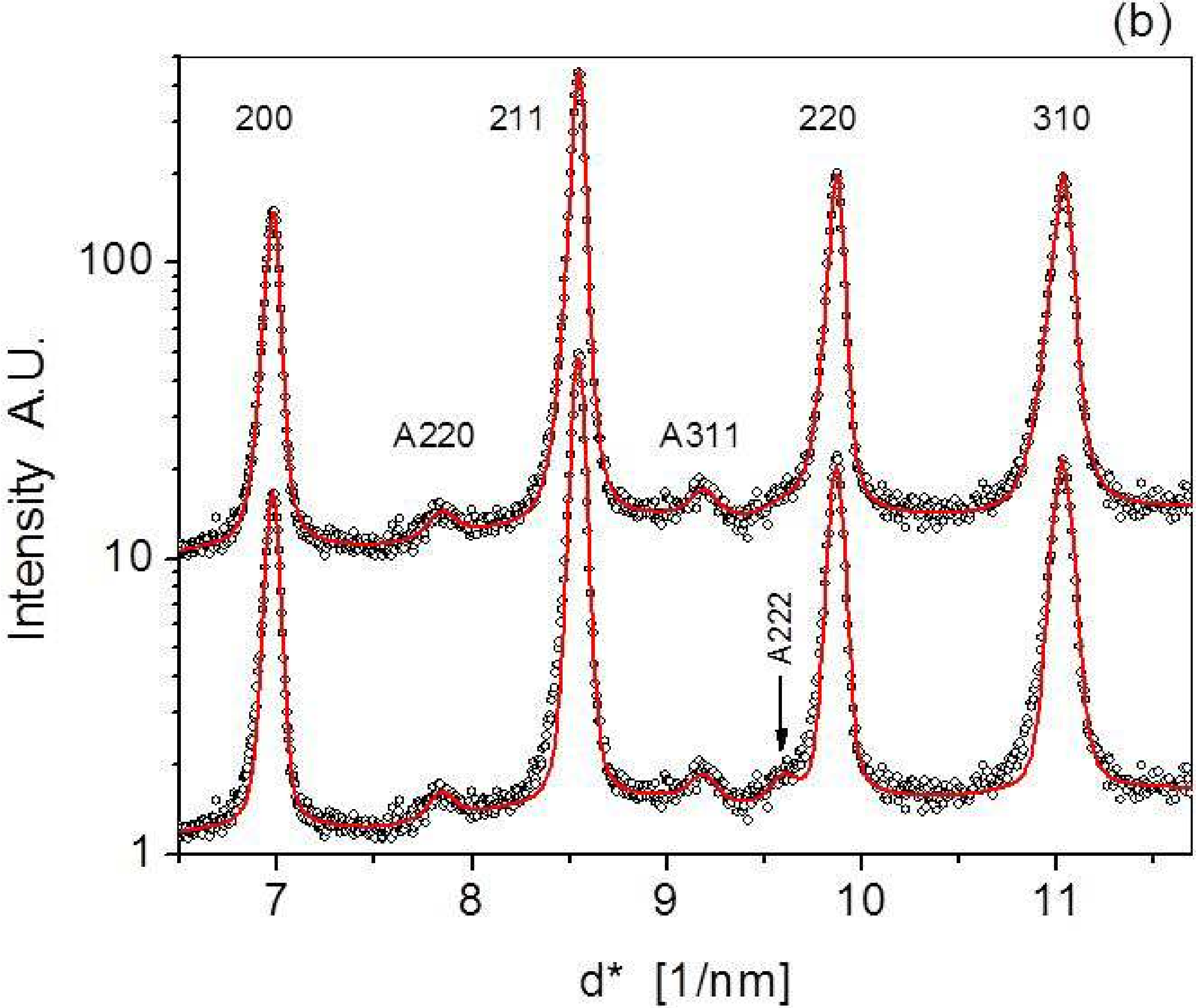
(b)
200
211
220
310
A220
A311
A222
Intensity A.U.
100
10
1
7
8
9
10
11
d* [1/nm]

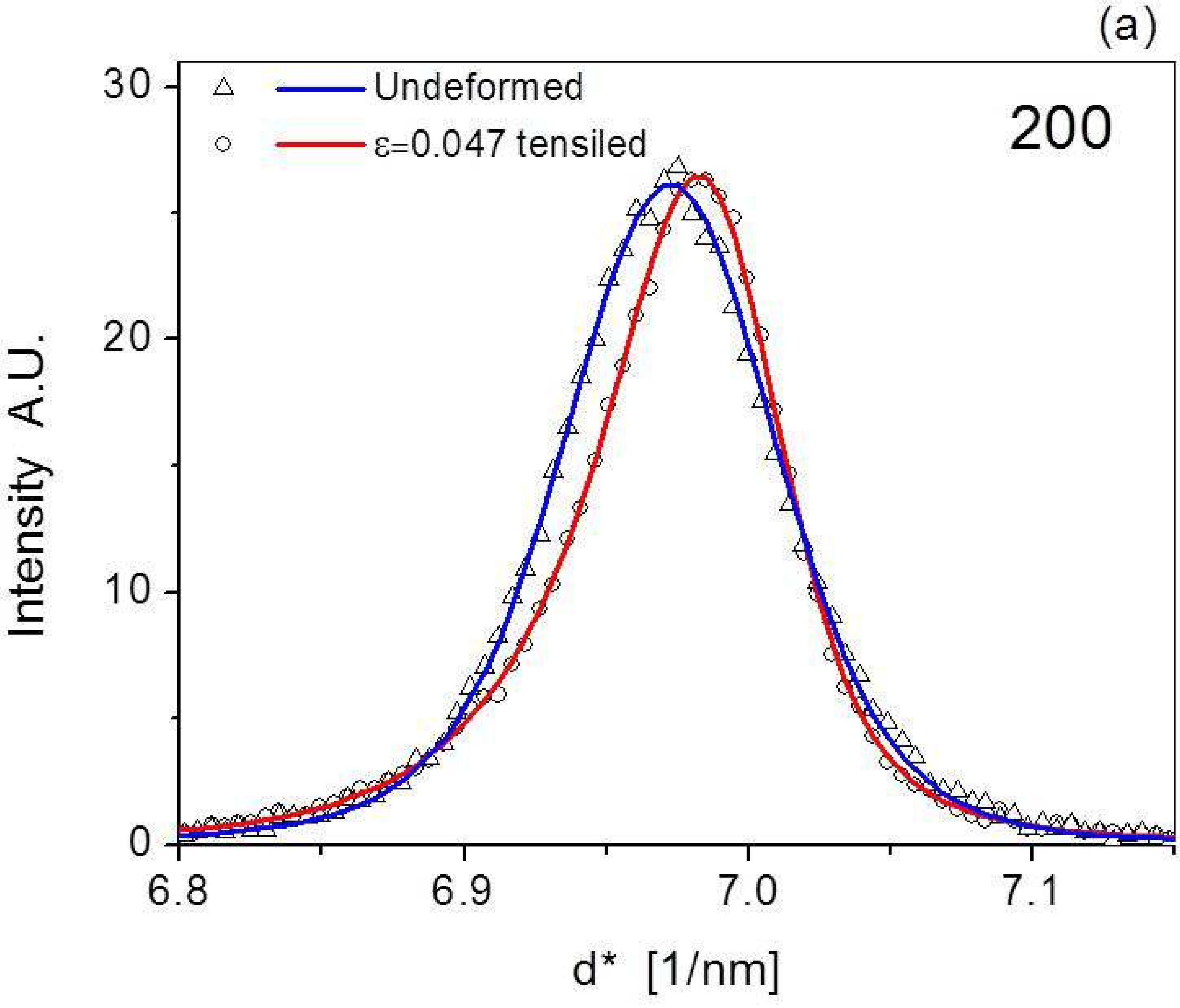
(a)
Undeformed
ε=0.047 tensiled
200
30
20
10
0
Intensity A.U.
6.8
6.9
7.0
7.1
d* [1/nm]

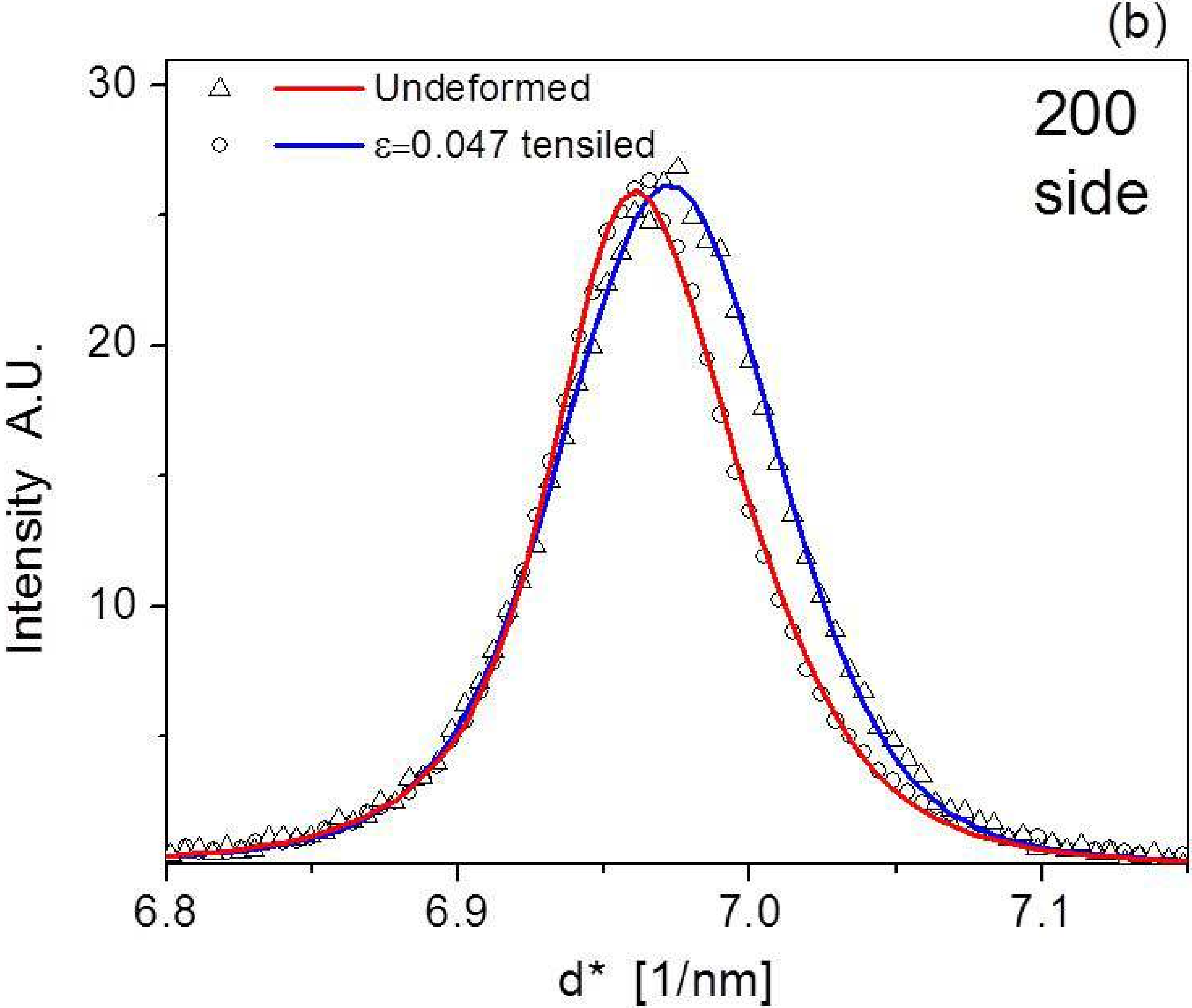

(b)
Undeformed
ε=0.047 tensiled
200
side
Intensity A.U.
d* [1/nm]
30
20
10
6.8
6.9
7.0
7.1

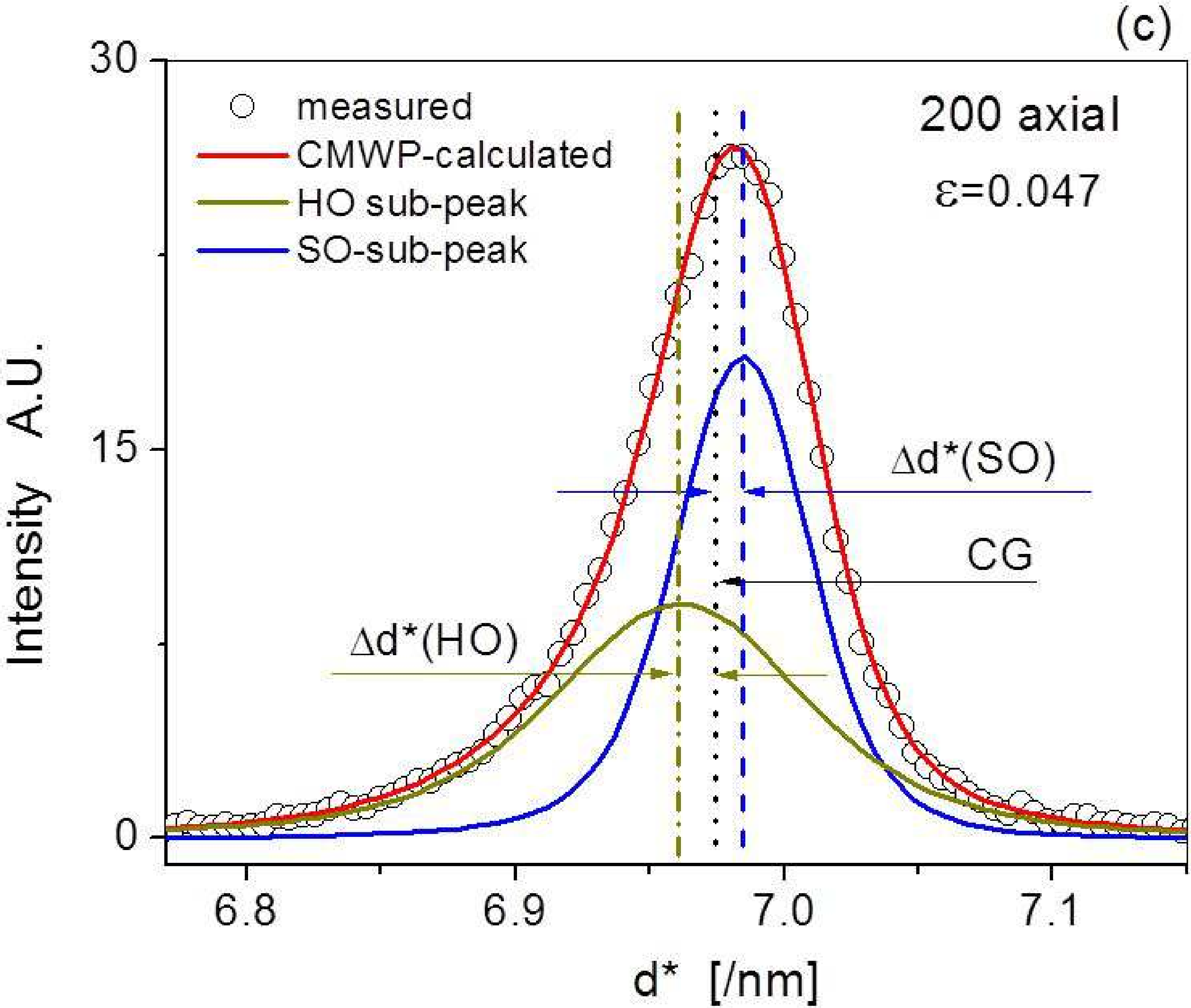

(c)
measured
CMWP-calculated
HO sub-peak
SO-sub-peak
200 axial
ε=0.047
Δd*(SO)
CG
Δd*(HO)
Intensity A.U.
30
15
0
6.8
6.9
7.0
7.1
d* [/nm]

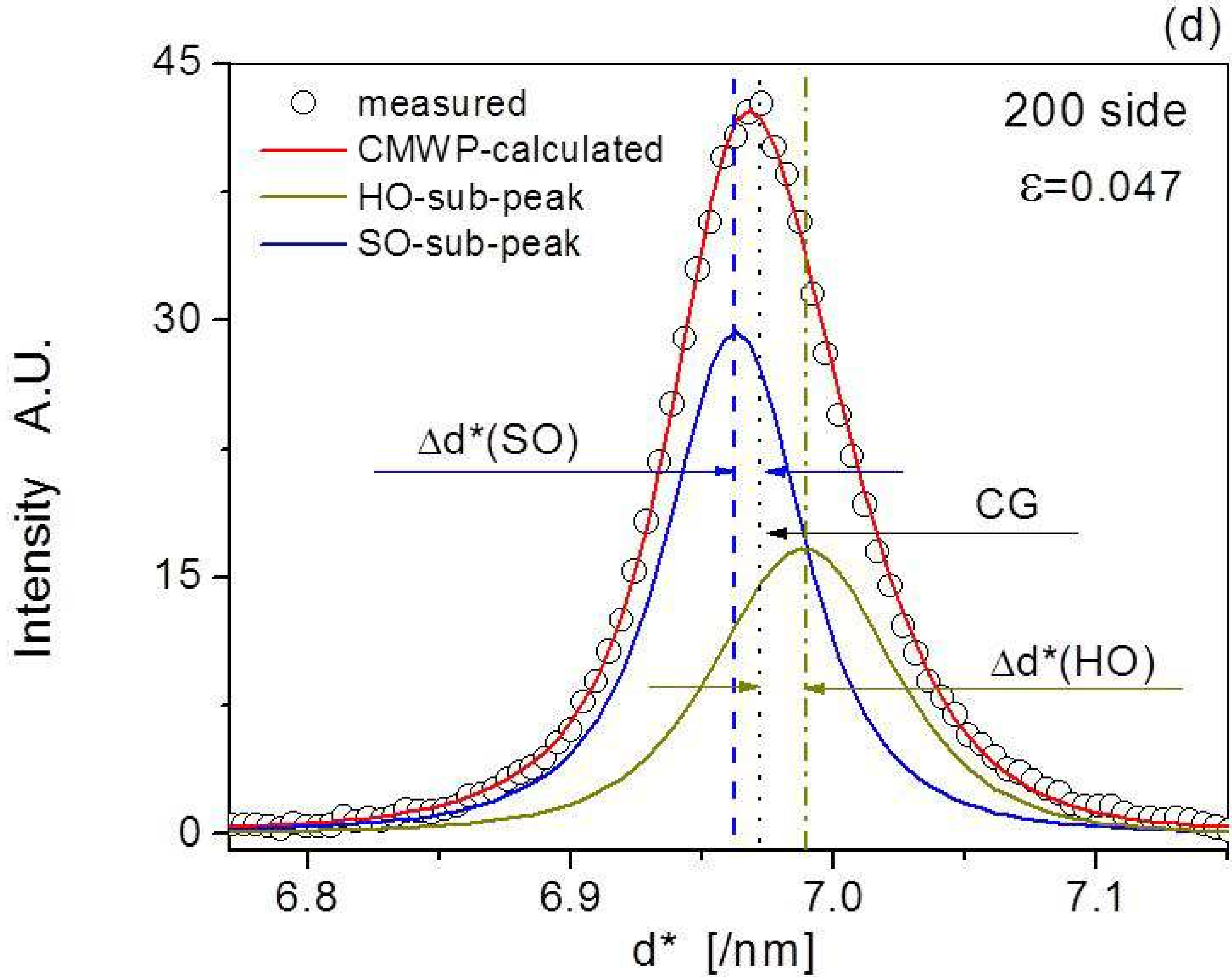

(d)
measured
CMWP-calculated
HO-sub-peak
SO-sub-peak
200 side
ε=0.047
Δd*(SO)
CG
Δd*(HO)
45
30
15
0
Intensity A.U.
6.8
6.9
7.0
7.1
d* [/nm]

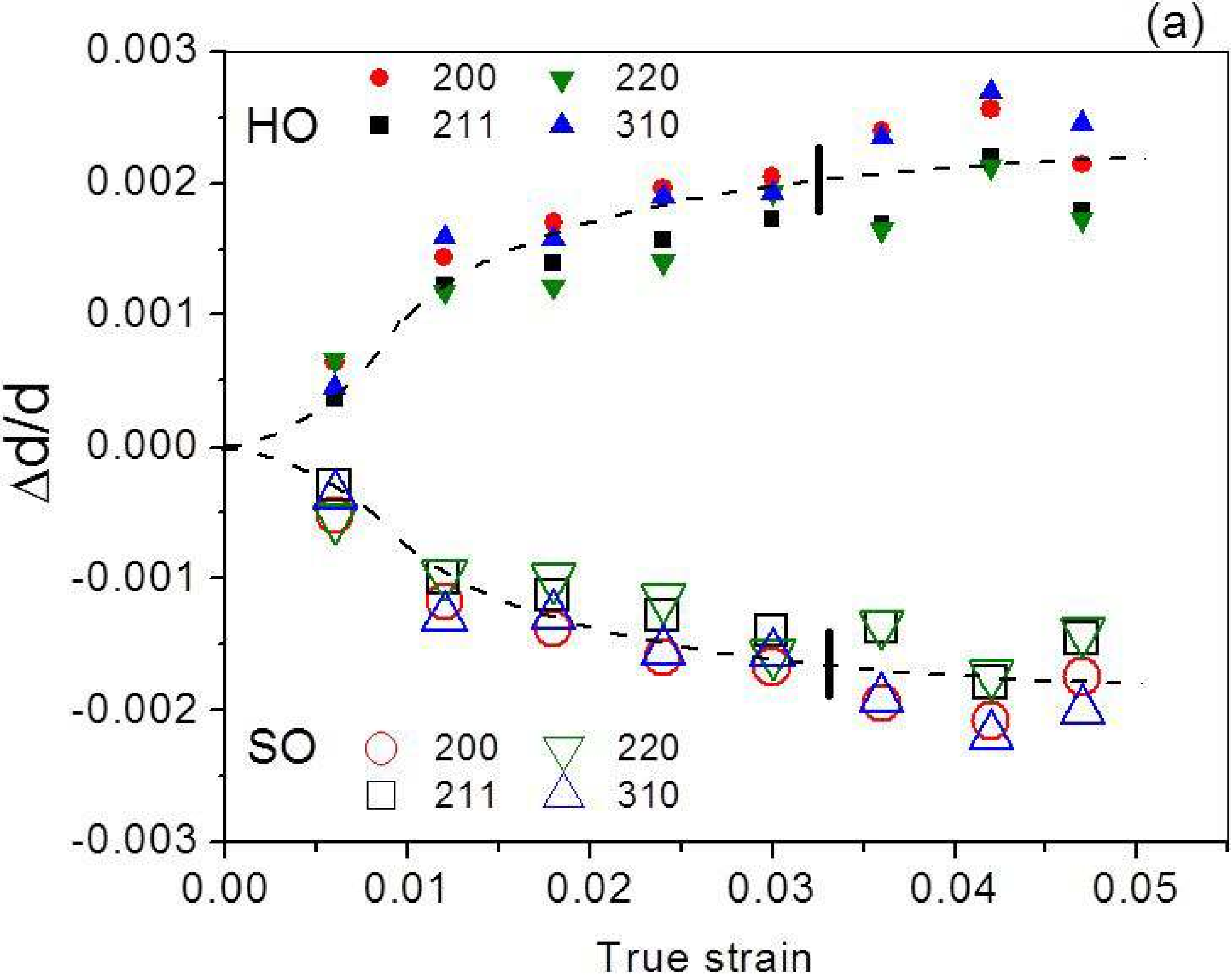
(a)
HO
200
211
220
310
SO
200
211
220
310
0.003
0.002
0.001
0.000
-0.001
-0.002
-0.003
Δd/d
0.00
0.01
0.02
0.03
0.04
0.05
True strain

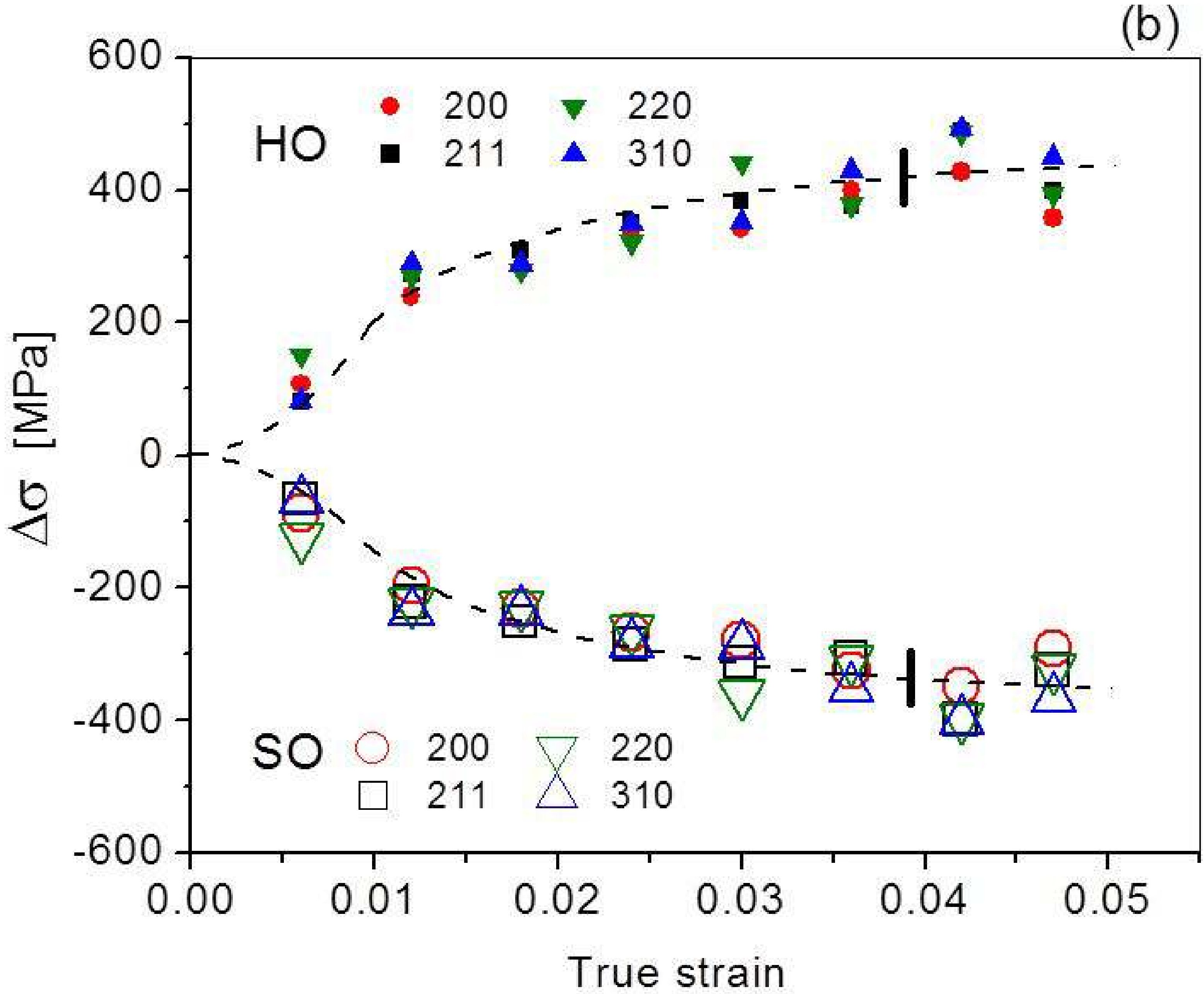
(b)
600
400
200
0
-200
-400
-600
Δσ [MPa]
HO
200
211
220
310
SO
200
211
220
310
0.00
0.01
0.02
0.03
0.04
0.05
True strain

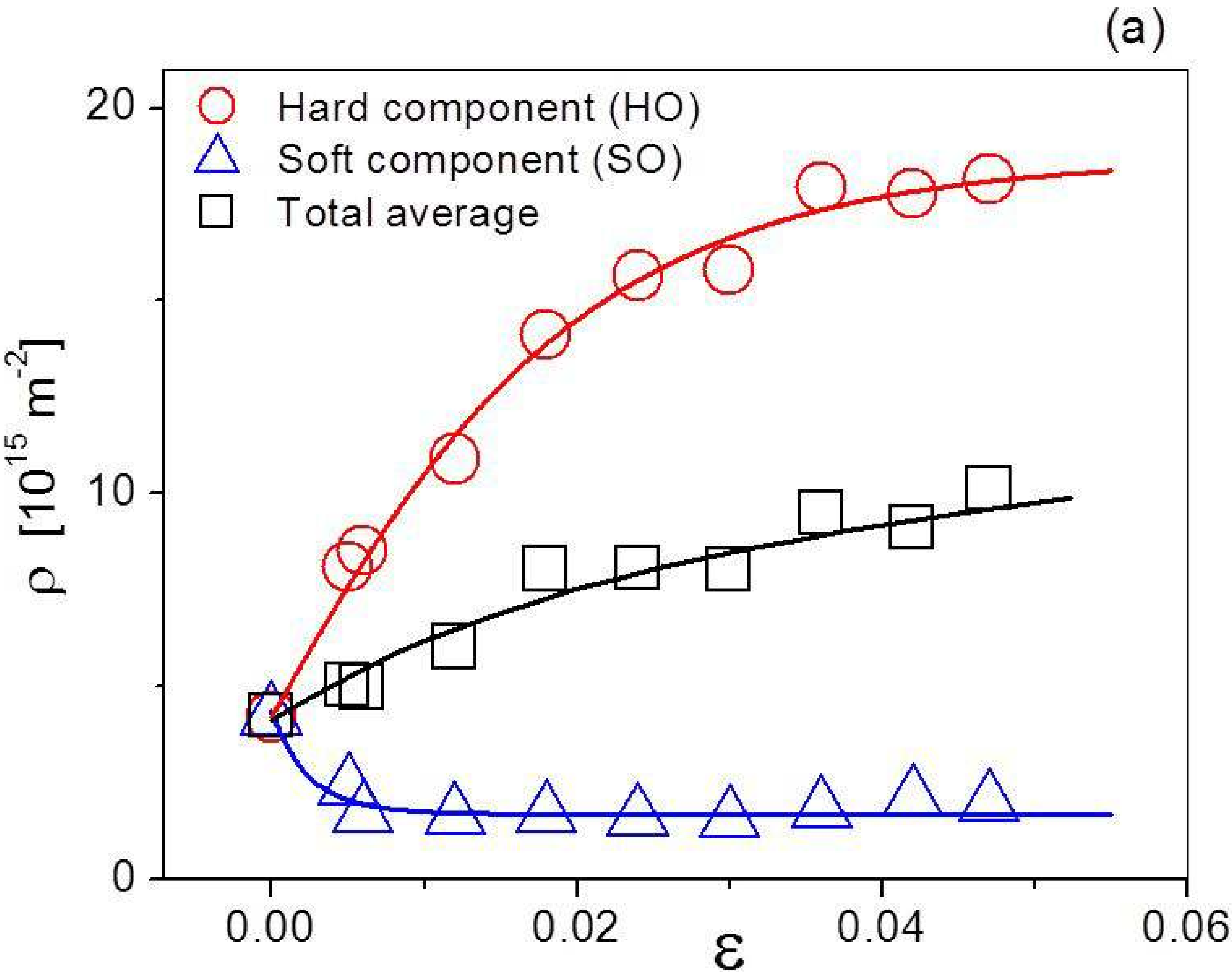
(a)
Hard component (HO)
Soft component (SO)
Total average
20
10
0
ρ [10^15 m^-2]
0.00
0.02
0.04
0.06
ε

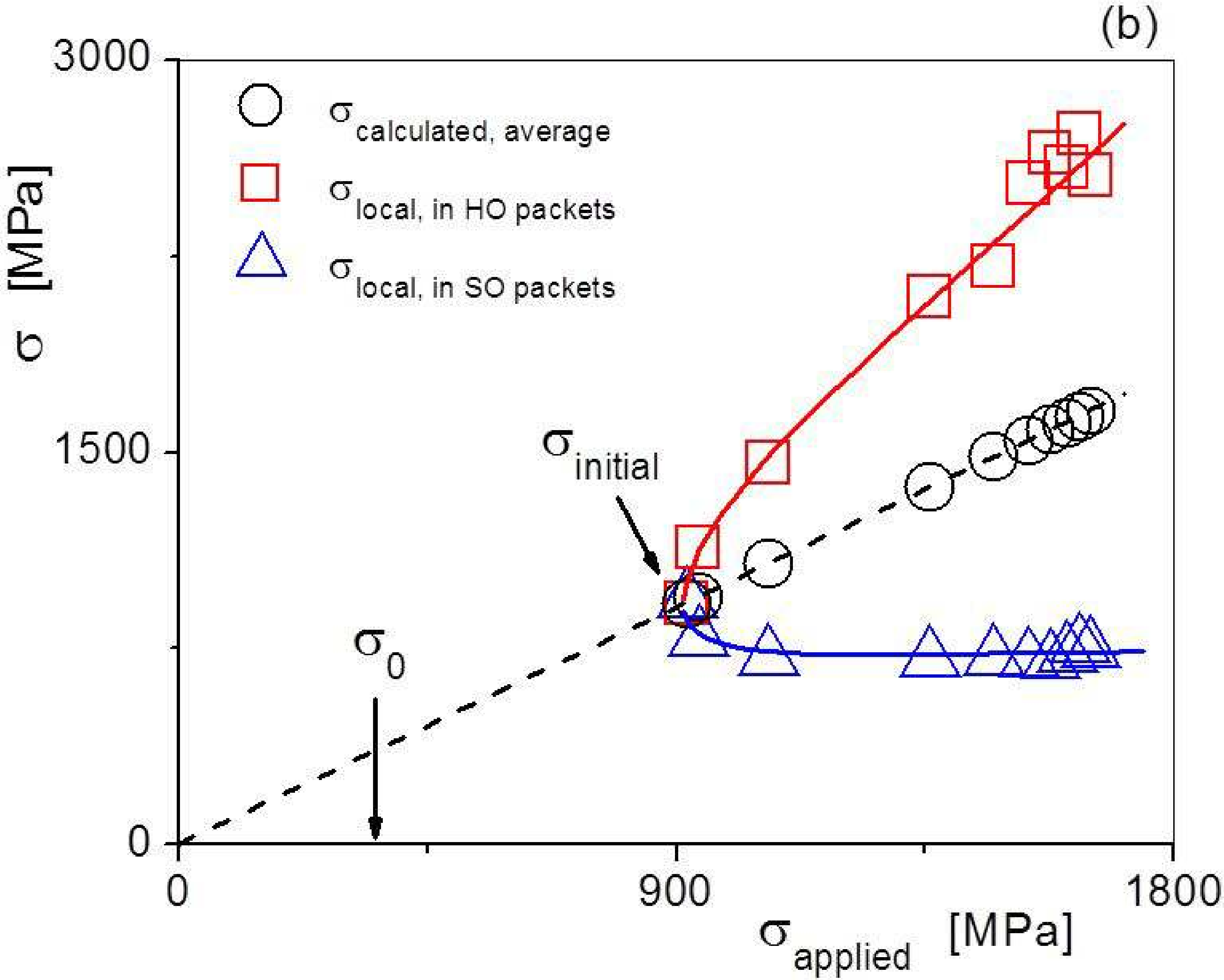

(b)
3000
1500
0
0
900
1800
σ [MPa]
σ_applied [MPa]
σ_calculated, average
σ_local, in HO packets
σ_local, in SO packets
σ_initial
σ_0

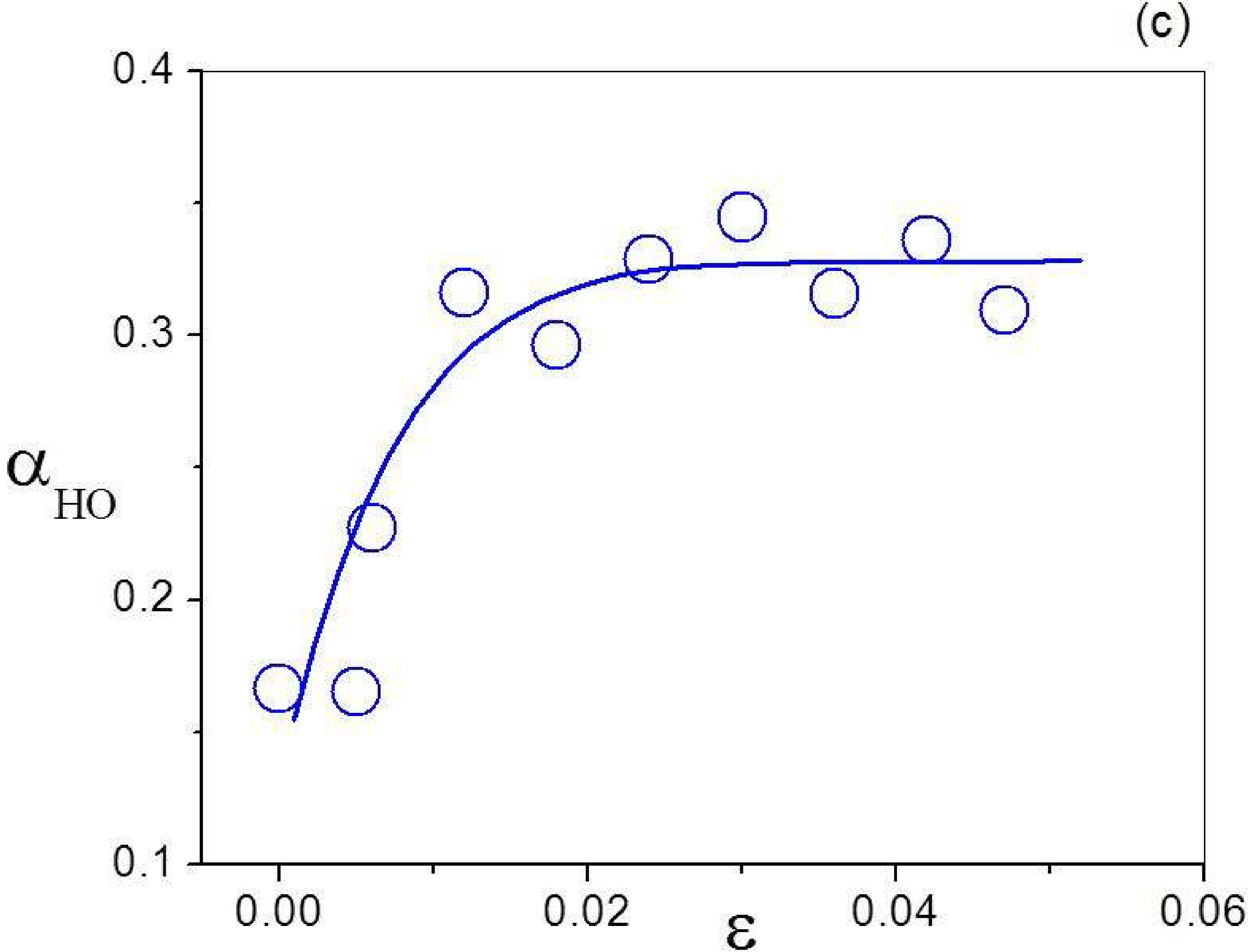
(c)
0.4
0.3
0.2
0.1
α_{HO}
0.00
0.02
0.04
0.06
ε

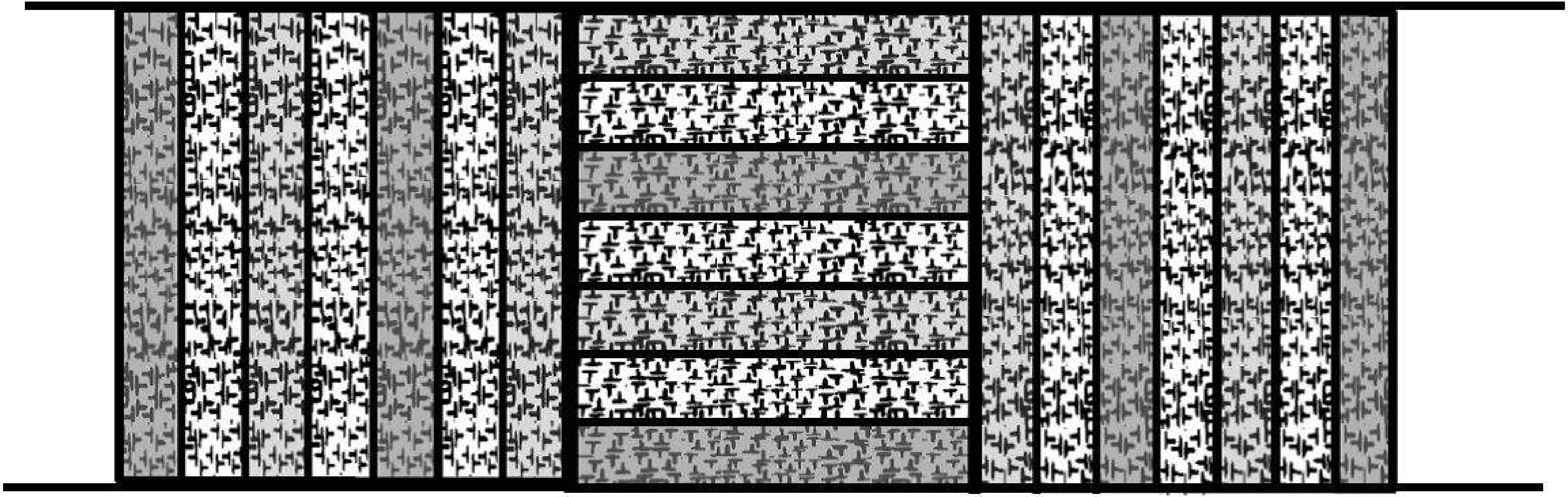

(a)

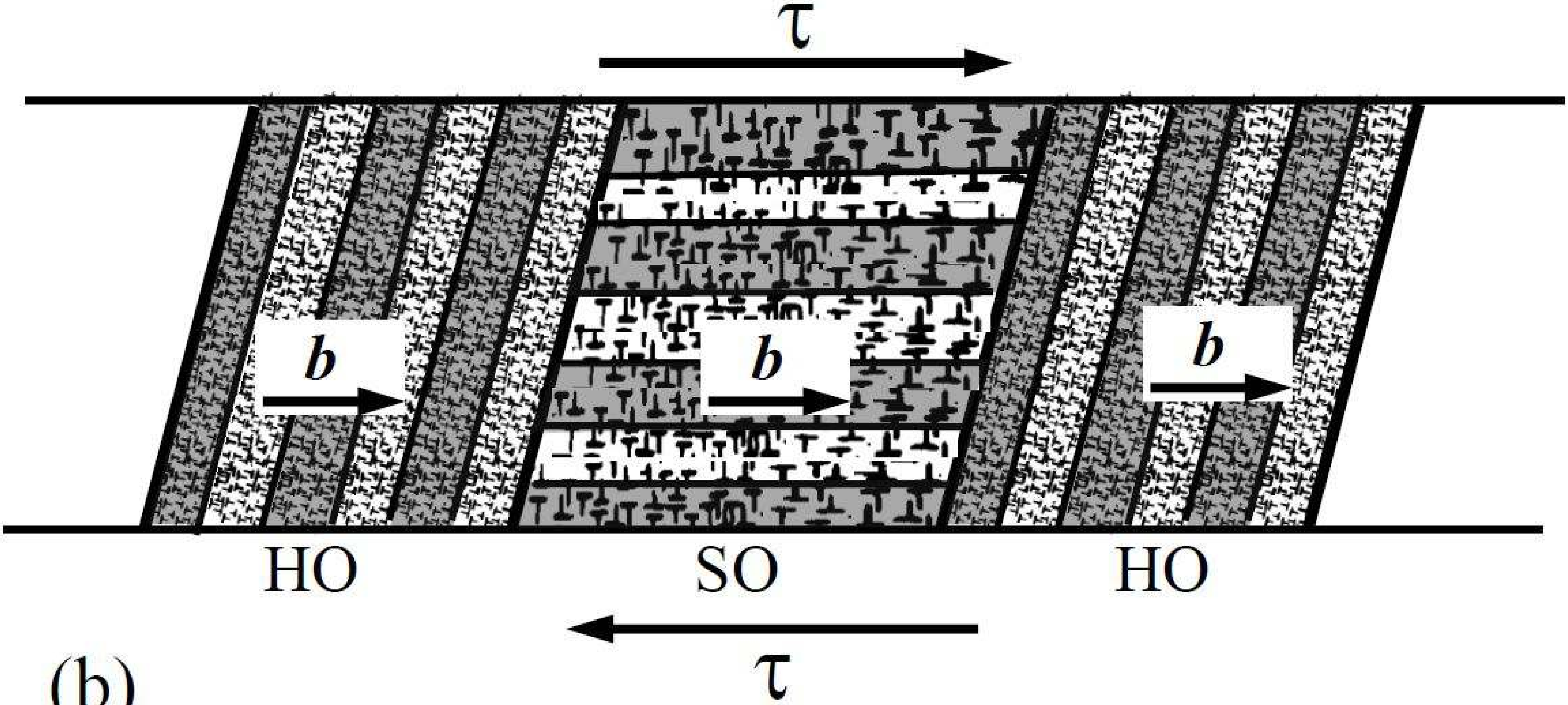

(b)

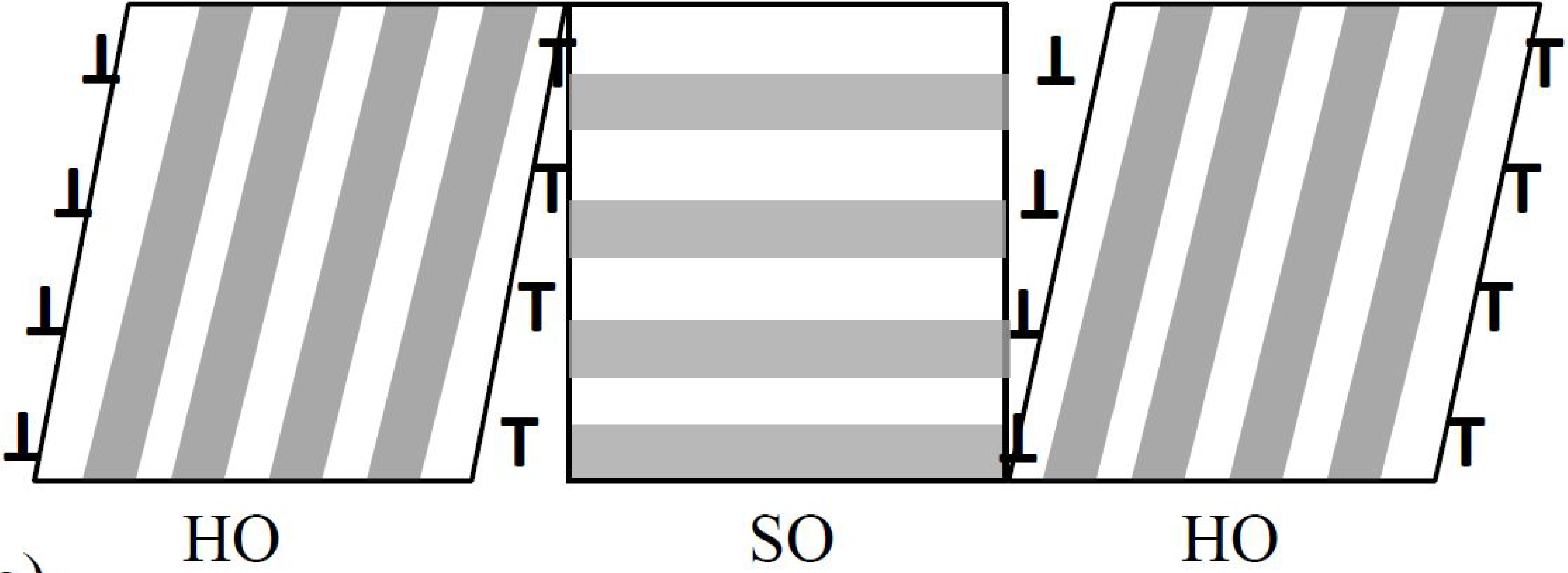

(c)

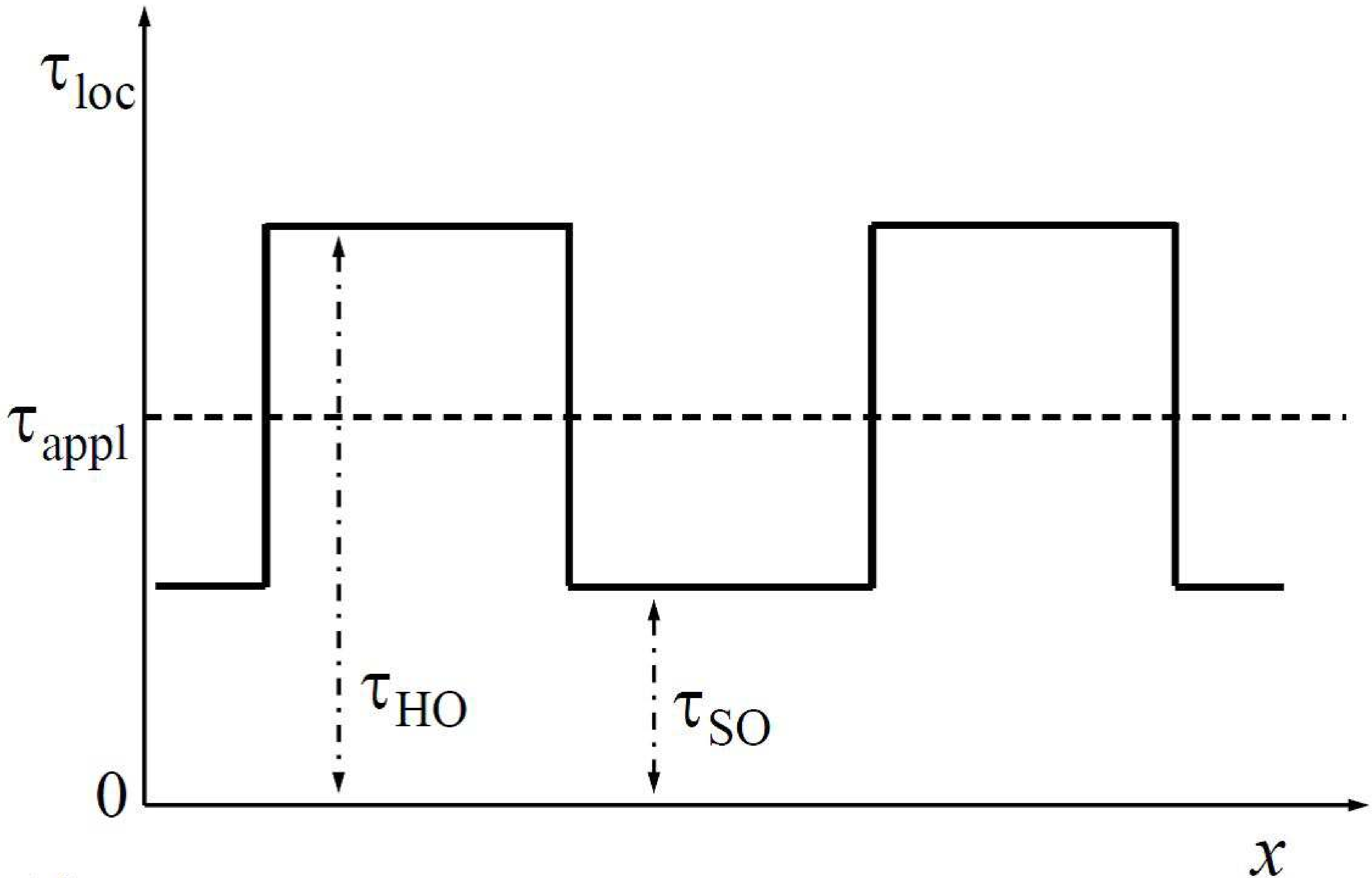

(d)